Radiative transfer model for the computation of radiance and polarization in an ocean–atmosphere system: polarization properties of suspended matter for remote sensing

Malik Chami, Richard Santer, and Eric Dilligeard

A radiative transfer code termed OSOA for the ocean–atmosphere system that is able to predict the total and the polarized signals has been developed. The successive-orders-of-scattering method is used. The air–water interface is modeled as a planar mirror. Four components grouped by their optical properties, pure seawater, phytoplankton, nonchlorophyllose matter, and yellow substances, are included in the water column. Models are validated through comparisons with standard models. The numerical accuracy of the method is better than 2%; high computational efficiency is maintained. The model is used to study the influence of polarization on the detection of suspended matter. Polarizing properties of hydrosols are discussed: phytoplankton cells exhibit weak polarization and small inorganic particles, which are strong backscatterers, contribute appreciably to the polarized signal. Therefore the use of the polarized signal to extract the sediment signature promises good results. Also, polarized radiance could improve characterization of aerosols when open ocean waters are treated.

OCIS codes: 010.4450, 280.0280, 260.5430, 030.5620.

1. Introduction

Remote sensing of oceanic waters provides information about suspended matter. Of the various types of suspended matter present in seawater, phytoplankton is the primary contributor to global biological production in the ocean and, therefore, to the carbon cycle. The number of remote-sensing measurements of ocean color continues to increase. The first objective of these measurements is the retrieval of the chlorophyll *a* concentration in open (case 1) and coastal (case 2) waters. Because of the predominance of the atmospheric component, atmospheric correction is a first critical task. A theoretical background is provided by resolution of the radiative transfer equation (RTE) for the atmosphere. At sea level the boundary conditions correspond to a Lambertian reflector [describing the in-water and foam (sea-surface) contributions to the background] and to the Fresnel reflection, assuming a flat ocean (specular reflection) or a rough surface (sun glint) for which the Cox–Munk[1] model for wave slope distribution is generally assumed. An interpretation of remotely sensed ocean color data can be made by empirical approaches, among which is the well-known blue–green ratio technique. Theoretical approaches have been studied by several authors.[2–6] The RTE for an oceanic system is solved by use of the system's optical properties (absorption and scattering). Ocean color is directly related to the value of the water-leaving spectral radiance. These models are also used to develop simple formulations of the relation of marine reflectance to backscattering and absorption coefficients as well as to model bidirectional remote-sensing reflectance.[7,8] For ocean case 2 waters, RTE codes are generally used to simulate the signal at different wavelengths as training sets for inverse methods such as use of a neural network.

Because of the coupling between atmospheric and ocean systems, the RTE has been solved for the global system[9–12] mainly to improve the modeling of bidi-

The authors are with the Unité Propre de Recherche de l'Enseignement Superieur Associee, Centre National de la Recherche Scientifique 8013, Ecosystème Littoraux et Côtiers, Laboratoire Interdisciplinaire des Sciences de l'Environnement, Université du Littoral Côte d'Opale, 32 avenue Foch, 62930 Wimereux, France. The e-mail address for M. Chami is chami@mren2.univ-littoral.fr.

Received 25 July 2000; revised manuscript received 5 February 2001.

0003-6935/01/152398-19$15.00/0

rectional remote-sensing reflectance. The increasingly better performance of the new generation of ocean color sensors implies a more sophisticated description of the signal in which the full radiation field (i.e., including polarization) is accounted for. For example, Gordon and Zhang[13] demonstrated the need to include Rayleigh polarization in the computation of atmospheric path radiance.

Following this approach, a new radiative transfer model for the global ocean–atmosphere system has been developed. This model predicts the total and the polarized signals at the top of the atmosphere and at the ocean–atmosphere boundary. A radiative transfer code based on the successive-orders-of-scattering method was available for the atmospheric layer only.[14] This code was modified to account for various oceanic parameters. In the first part of this paper we provide a description of the new ocean–atmosphere radiative transfer model (called the OSOA code). In particular, attention is given to computation of the polarized component of the signal in the oceanic layer. In the second part of the paper we describe applications of the code to remote sensing of coastal and open ocean waters. The influence of marine particles on the polarization of water-leaving radiance is discussed.

2. Description of the OSOA Code

A. Background: The Atmospheric Code

A radiative transfer model developed at the Laboratoire d'Optique Atmosphérique of the University of Lille[14] was available for application to the atmospheric layer only. The geometric parameters of the model are described in Fig. 1. In this model Stokes vector L is expanded into a Fourier series with respect to the azimuth angle, and a successive-orders-of-scattering solution is carried out:

$$L(\mu_0, \mu_v, \phi) = \sum_{s=0}^{\infty} (2 - \delta_{0s}) L^{(s)}(\mu_0, \mu_v)\cos(s\phi) = \sum_{s=0}^{\infty} (2 - \delta_{0s}) L^{(s)}(\mu_0, \mu_v)\sin(s\phi), \quad (1)$$

where δ_{0s} is the Kronecker delta function, defined as follows:

$$\delta_{0s} = \begin{cases} 1 & s = 0 \\ 0 & s \neq 0 \end{cases}.$$

In the above expressions the subscript s corresponds to the Fourier series expansion, μ is the cosine of zenith angle θ (by convention, the downward direction corresponds to $\mu < 0$ and the upward direction to $\mu > 0$), and the subscripts 0 and v stand for solar and viewing angles, respectively. The cosine of the difference in azimuth Φ is applied to the first two Stokes parameters, I and Q, whereas the sine is applied to the last two Stokes parameters, U and V. Actually, the Stokes vector is reduced to the first three parameters, I, Q, and U, because ellipticity V is negligible. This expansion permits a separation of the angular

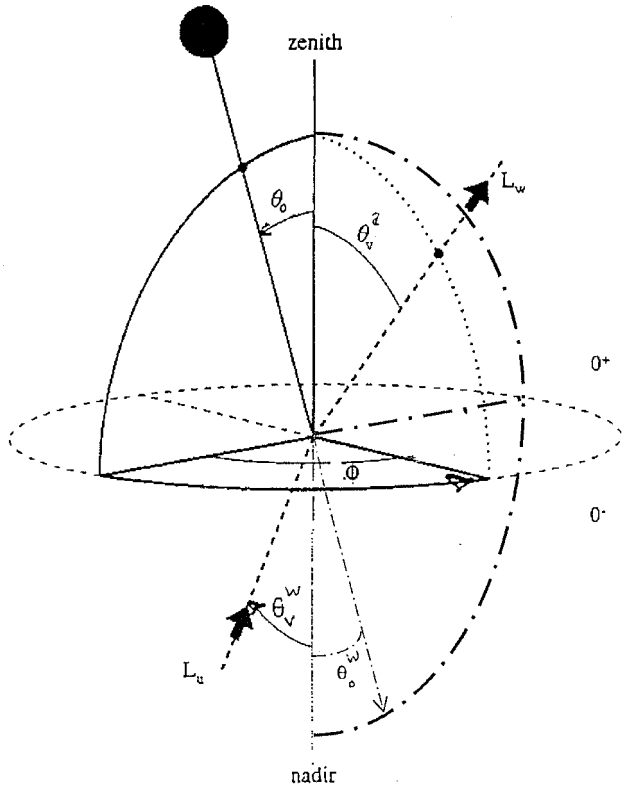

Fig. 1. Geometric parameters: θ, zenith angle; 0, v, and a, w, solar and viewing angles and air and water, respectively. The angular relationship between air and water follows the Descartes–Snell law. ϕ is the difference in azimuth between the viewing and the solar planes.

variables Φ and θ during the integration of the RTE (see Subsection 8.3 of Ref. 15). As a result, the set of equations depends only on zenith angle θ. The radiance is computed for each term of the Fourier series. An added benefit of this method of solution is that the series term $s = 0$ directly provides the scattered flux and then provides the diffuse marine reflectance as well as the photosynthetically active radiation.

To simplify the numerical computations, scattering matrix $\tilde{M}$ is expanded in Legendre polynomials. This is possible because scattering is azimuthally symmetric about the incident direction. The phase function (matrix term M_{11}) can therefore be expressed as follows:

$$M_{11}(\mu) = \sum_{l=0}^{NB} \beta_l P_l(\mu), \quad (2a)$$

$$\beta_l = \frac{2l + 1}{2} \int_{-1}^{1} M_{11}(\mu) P_l(\mu) d\mu, \quad (2b)$$

where $P_l(\mu)$ are the Legendre polynomials and β_l are the development coefficients calculated relative to the orthogonality of the Legendre polynomials. The length of the Fourier series is influenced by the number of Legendre terms (NB) used to describe the phase matrix. This Legendre expansion allows one

simply to convert, for each Fourier series term and for each optical depth τ, the (3×3) scattering matrix $\tilde{M}$ expressed in the scattering plane into the required formulation for the RTE in the incident and viewing meridian planes (see Ref. 14 for details).

The upward and downward radiance contributions to the computations that arise from primary scattering are expressed, respectively, as follows:

$$L^{\uparrow(s)}(\tau, \mu_v, \mu_0) = \omega_a \tilde{E}_0 \int_{\tau_l}^{\tau} \exp\left(+\frac{t}{\mu_0}\right) \times \exp\left(-\frac{t-\tau}{\mu_v}\right) \frac{\tilde{M}^{(s)}(t, \mu_v, \mu_0)}{4\pi\mu_v} \, dt, \tag{3}$$

$$L^{\downarrow(s)}(\tau, \mu_v, \mu_s) = \omega_a \tilde{E}_0 \int_{0}^{\tau} \exp\left(+\frac{t}{\mu_0}\right) \times \exp\left(+\frac{\tau-t}{\mu_v}\right) \frac{\tilde{M}^{(s)}(t, \mu_v, \mu_0)}{4\pi\mu_v} \, dt, \tag{4}$$

where τ_l is the total optical depth of the medium and ω_a is the single-scattering albedo. Stokes vector $\tilde{E}_0(E_0, 0, 0)$ for the incident solar beam is unpolarized, and E_0 is the extraterrestrial irradiance.

In multiple scattering, the radiance contribution for order n arises from the signal for order $n - 1$. For a given order, the signal is integrated over zenith angles μ and optical depth τ. For example, the upward radiance is computed as

$$L_n^{\uparrow(s)}(\tau, \mu_v, \mu_0) = \omega_a \int_{\tau_l}^{\tau} \exp\left(-\frac{t}{\mu_v}\right) \int_{-1}^{+1} L_{n-1}^{(s)}(t, \mu_v, \mu') \times \frac{\tilde{M}^{(s)}(t, \mu_v, \mu')}{4\pi\mu_v} \, d\mu' dt. \tag{5}$$

The integration with respect to μ is performed with a Gaussian quadrature; the integration with respect to τ is accomplished by division of the atmosphere layer into N layers,[16] each of which has the same optical thickness. Inasmuch as the aerosols and molecules in the atmosphere do not have the same vertical distribution (typically modeled as being exponential with a 2-km scale factor for aerosols and an 8-km scale factor for molecules), the N layers are nonhomogeneous. In practice, the higher the value of N, the more accurate the results of the numerical integration in τ. However, the associated computational time also increases with N. The current research makes use of an atmosphere discretized into 26 layers, in accordance with the sensitivity studies performed by Deuzé.[16]

For a given order s of the Fourier series, the iterative process over the orders of scattering can be stopped when either of two tests is satisfied. The first test compares the radiance contribution at order n with the sum of the contributions from all previous orders. For the iterations to stop, the ratio must be less than 10^{-5}:

$$\left| \frac{L_n^{(s)}}{\sum_{i=0}^{n-1} L_i^{(s)}} \right| < 10^{-5}. \tag{6}$$

The second test examines whether the radiance contributions from successive orders of scattering converge in a geometric series. If they do, the iterations are halted and the tail of the geometric series is added to the contribution to the process of the scattering order at which the convergence was detected. In practice, this test is often administered first, and it greatly reduces the overall computation time. Mathematically, convergence is obtained at order n when the ratio of the current order's contribution to the previous order's contribution becomes constant to within a factor of 10^{-2}, i.e.,

$$\left| \frac{L_n^{(s)}}{L_{n-1}^{(s)}} - \frac{L_{n-1}^{(s)}}{L_{n-2}^{(s)}} \right| < 10^{-2}. \tag{7}$$

B. Primary Scattering in the OSOA Code

In the successive-orders method proposed by Deuzé *et al.*[14] the boundary condition corresponds to a rough ocean. A quite sophisticated Fourier series expansion of the reflection matrix convoluted by the wave slope distribution function is achieved. A similar approach should be developed for the transmission matrix. For the current study the interface is considered to be planar. The roughness of the sea is therefore not taken into consideration.

The Snell–Descartes laws are used to model the boundary conditions through the air–water interface. The refractive index of seawater is assumed to be $n_w = 1.34$; the refractive index of air is assumed to be unity. For a planar surface, the coefficients of reflection are given by Fresnel formulas

$$r_\perp = \frac{\sin^2(\theta_a - \theta_w)}{\sin^2(\theta_a + \theta_w)} \quad \text{(perpendicular plane)}, \tag{8}$$

$$r_{/\!/} = \frac{\tan^2(\theta_a - \theta_w)}{\tan^2(\theta_a + \theta_w)} \quad \text{(parallel plane)}, \tag{9}$$

where θ_a and θ_w are, respectively, the zenith angles in the air and in the water.

In the OSOA code we account for the polarization of the radiance signal that is due to the specular reflection at the air–water interface by treating radiance as a vector. So reflection matrix R on the water surface and transmission matrix T from air to water are derived from Eqs. (8) and (9):

$$R = \frac{1}{2} \begin{bmatrix} \mathbf{r}_{/\!/}^2 + \mathbf{r}_\perp^2 & \mathbf{r}_{/\!/}^2 - \mathbf{r}_\perp^2 & \mathbf{0} \\ \mathbf{r}_{/\!/}^2 - \mathbf{r}_\perp^2 & \mathbf{r}_{/\!/}^2 + \mathbf{r}_\perp^2 & \mathbf{0} \\ \mathbf{0} & \mathbf{0} & 2\mathbf{r}_\perp \mathbf{r}_{/\!/} \end{bmatrix}, \tag{10}$$

$$T = \frac{1}{2} \frac{n_w \cos\theta_w}{\cos\theta_a} \begin{bmatrix} \mathbf{t}_{/\!/}^2 + \mathbf{t}_\perp^2 & \mathbf{t}_{/\!/}^2 - \mathbf{t}_\perp^2 & \mathbf{0} \\ \mathbf{t}_{/\!/}^2 - \mathbf{t}_\perp^2 & \mathbf{t}_{/\!/}^2 + \mathbf{t}_\perp^2 & \mathbf{0} \\ \mathbf{0} & \mathbf{0} & 2\mathbf{t}_{/\!/} \mathbf{t}_\perp \end{bmatrix}, \tag{11}$$

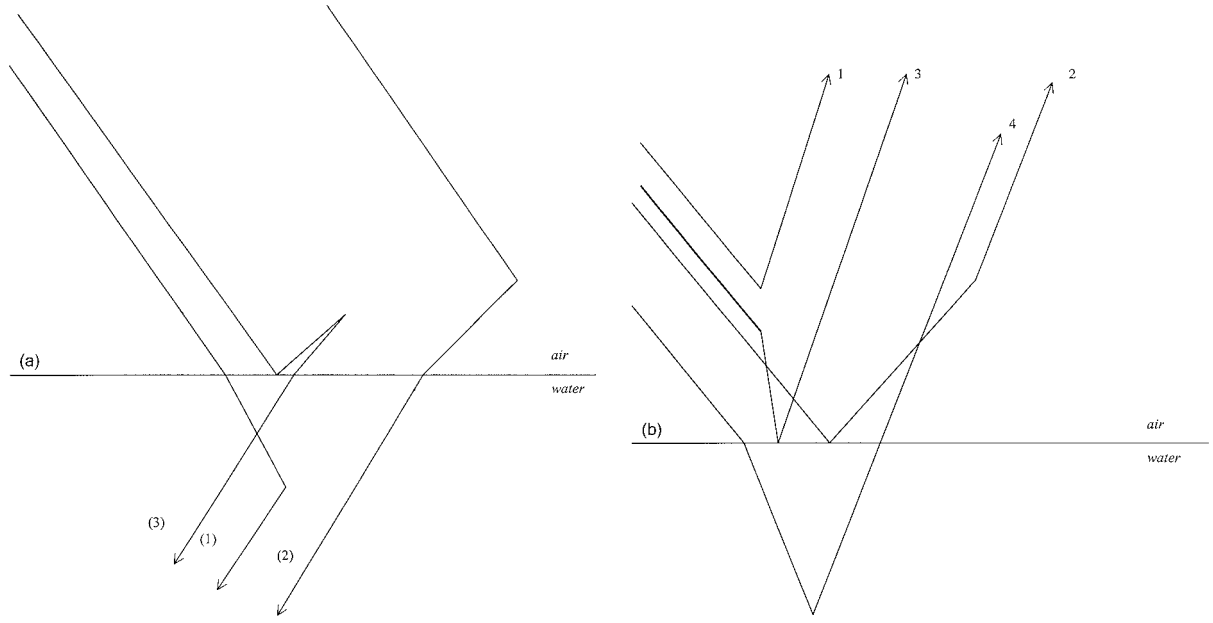

Fig. 2. (a) Schematic description of primary scattering for atmospheric upward radiance: (1) primary scattering atmospheric radiance [see Eq. (3)], (2) forward scattering of the reflected solar beam [see Eq. (12)], (3) reflection by the air–water interface of the primary scattering of atmospheric radiance, and (4) water-leaving radiance. (b) Schematic description of primary scattering for in-water downward radiance: (1) primary scattering of the in-water radiance, (2) transmitted primary scattering of the atmospheric radiance, and (3) backward atmospheric scattering.

where

$$t_{/\!/} = \frac{2 \sin \theta_w \cos \theta_a}{\sin(\theta_a + \theta_w)\cos(\theta_a - \theta_w)},$$

$$t_{\perp} = \frac{2 \sin \theta_w \cos \theta_a}{\sin(\theta_a + \theta_w)}.$$

These matrices are expressed in the reflection plane, which is also the meridian plane. For specular reflection, however, the terms of the Fourier series expansion are constant. Therefore these matrices [Eqs. (10) and (11)] correspond to the Fourier series terms.

Terms that describe the specular reflection at the planar air–water interface, which are the second source for the primary scattering, are expressed as follows:

$$L^{\uparrow(s)}(\tau, \mu_v, \mu_0) = \omega_a R(\theta_0)\tilde{E}_0 \exp\left(\frac{\tau_l}{\mu_0}\right) \int_{\tau_l}^{\tau} \exp\left(\frac{\tau_l - t}{\mu_0}\right) \times \exp\left(-\frac{t - \tau}{\mu_v}\right) \frac{\tilde{M}^{(s)}(t, \mu_v, \mu_0)}{4\pi\mu_v} \, dt, \tag{12}$$

$$L^{\downarrow(s)}(\tau, \mu_v, \mu_0) = \omega_a R(\theta_0)\tilde{E}_0 \exp\left(\frac{\tau_l}{\mu_0}\right) \int_{0}^{\tau} \exp\left(\frac{\tau_l - t}{\mu_0}\right) \times \exp\left(+\frac{\tau - t}{\mu_v}\right) \frac{\tilde{M}^{(s)}(t, \mu_v, \mu_0)}{4\pi\mu_v} \, dt. \tag{13}$$

In water, the incident source is the solar irradiance after attenuation in the two media and transmission into the water. For example, the upward radiance in the water is expressed as follows:

$$L^{\uparrow(s)}(\tau, \mu_v, \mu_0) = \omega_a T(\theta_0)\tilde{E}_0 \exp\left(+\frac{\tau_l}{\mu_0}\right) \times \int_{\tau_l+\tau_w}^{\tau} \exp\left(+\frac{t - \tau_l}{\mu_0^w}\right) \exp\left(-\frac{t - \tau}{\mu_v^w}\right) \times \frac{\tilde{M}_w^{(s)}(t, \mu_v^w, \mu_0^w)}{4\pi\mu_v^w} \, dt, \tag{14}$$

where $\tilde{M}_w$ is the scattering matrix of the particles in the ocean.

The atmospheric path radiance is first the sum of the two terms given by Eqs. (3) and (12). The in-water upward radiance [Eq. (14)], computed just below the water surface, provides an additional contribution to the source of reflection after being transmitted [following Eq. (15)] through the interface and attenuated in the atmosphere:

$$L_a = T(\theta_w)(L_w/n_w^2). \tag{15}$$

For the downwelling in-water radiance, the atmospheric radiance at sea level is taken into account [Eqs. (4) and (13)]. Conversely, the radiance increases by a factor of n_w^2 in the air-to-water direction [Eq. (16)] before being attenuated in the water:

$$L_w = T(\theta_a)(n_w^2 L_a). \tag{16}$$

Figure 2 is a schematic description of the compo-

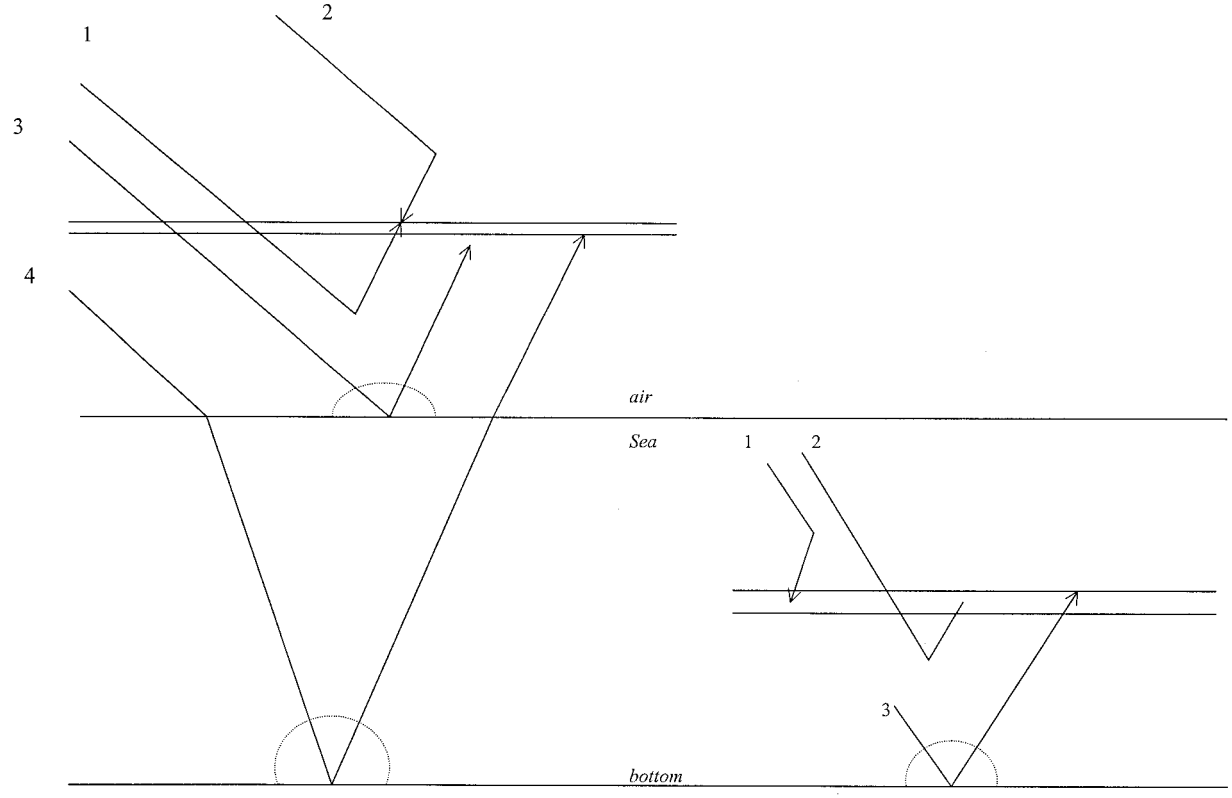

Fig. 3. Schematic description of sources for secondary scattering. (a) In the atmosphere: (1) upward radiance as described in Fig. 2(a), (2) primary scattering from the upper atmosphere, (3) Lambertian reflection of the direct solar beam by the sea surface (foam), and (4) Lambertian reflection of the direct solar beam by the sea bottom; (b) in the water: (1) downward radiance as described in Fig. 2(b), (2) primary scattering from the lower ocean, and (3) Lambertian reflection of the direct solar beam by the sea bottom.

nents of the primary scattering. In Fig. 2(a) the components of the upward atmospheric path radiance are drawn. The direct solar beam is the only source for the downward atmospheric path radiance, and Eq. (4) applies. In Fig. 2(b) the components of the downward water path radiance are drawn. For the upward water path radiance (not shown), the direct solar beam is the only source. The boundary conditions at the bottom of the atmosphere depend on the presence of the foam (sea surface), which is modeled as a Lambertian reflector. The boundary conditions for the ocean depend on the bottom, which is also modeled as a Lambertian reflector. Strictly speaking, the primary scattering should include the first interaction of the reflected solar beam with foam in the atmosphere and to the reflection from the sea bottom. Because of the isotropic nature of the reflected irradiance, Eqs. (12)–(14) do not apply. For numerical convenience, these terms will be computed in the multiple scattering module.

C. Multiple Scattering in the OSOA Code

The relevant equations are similar to Eq. (5), in which the source is the order $(n - 1)$ of the scattering radiance. For example, the second scattering in the air has for its sources the primary scattering as described in Subsection 2.B and the isotropic radiance reflected by foam and by the sea bottom. The last component is unpolarized and is introduced only for $s = 0$ (isotropy). Figure 3 illustrates the various sources of the second scattering in which the two Lambertian reflections have been added to the atmospheric primary scattering.

In an ocean–atmosphere system there are boundary conditions at the air–water interface as well as in each medium. Numerically, the interface can be modeled as an infinitely thin layer (optical depth of 10^{-7}). This would permit the application of Fresnel equations from one medium to another. Once the interface is crossed, because the refractive indices of air and water differ the refracted angles in the ocean will not correspond to the atmospheric Gaussian angles. These angles must therefore be readjusted (polynomial interpolation) to permit the use of Gaussian quadrature computations below the air–water interface.

Like the atmosphere, the ocean is discretized into a number of layers that have equal optical thickness but are not necessarily homogeneous. In this case, the homogeneity depends on the vertical profile of the in-water constituents. Because the ocean is optically denser than the atmosphere (the optical depth in the water could exceed 10), the number of layers required for accurate modeling of the oceanic radiative transfer is greater than the number required for purely atmospheric computations. Tests carried out with the assumption of a purely scattering ocean, an assumption that is admittedly unrealistic, have

shown that the calculation of the radiance is not significantly improved when discretization is greater than 80 layers.[17] For such nonabsorbing media, only a relative error of 0.9% is made when the signal is calculated with 80 instead of 300 layers. In natural waters, where absorption occurs, this error decreases and is negligible. Therefore the OSOA will be run with a nominal discretization of ocean into 80 layers.

3. Numerical Problems

A. Inputs and Outputs

The atmosphere corresponds to a mixture of molecules and aerosols. One aerosol model is selected, and its optical properties are derived from Mie theory. The OSOA requires the input of vertical profiles for the various oceanic constituents. Coastal zone waters contain a number of components that, for the purpose of remote sensing, can be grouped into four classes by their optical properties: pure seawater, inorganic suspended particles, phytoplankton pigments, and colored dissolved organic material (yellow substances, or *gelbstoff*) that consist primarily of polymerized humic and fulvic acids. Yellow substances are commonly assumed to be nonscattering materials. They are a major contributor to light absorption by nonchlorophyllose matter. In coastal waters, *gelbstoff* absorption is often significantly greater than that which is due to phytoplankton and therefore strongly influences ocean color. The absorption coefficient of *gelbstoff* decreases exponentially with wavelength.[18]

Phytoplankton has been studied for a long time. Bio-optical models have been developed[19,20] to associate its inherent properties with its concentration. Living phytoplankton usually has a lower refractive index than water. The model makes use of Mie theory (with refractive index $m = 1.05$) to compute a phase function for phytoplankton. The size distribution is modeled according to a Junge power law with a slope ν that ranges from -3 to -4 ($0.1\ \mu\text{m} < r < 50\ \mu\text{m}$), which is consistent with commonly observed values for marine particles in the open ocean.[21] Nonchlorophyllose suspended matter is often observed in high concentrations in the vicinity of river runoff (river plumes) and near coastlines because of the resuspension of sediments. Such suspended mineral particles have large scattering coefficients and, depending on their chemical composition, could also contribute to absorption.[22,23] We are aware of no bio-optical models that relate their concentration to their scattering coefficients. The model uses Mie theory with a refractive index $m = 1.20 - 0.001j$ (relative to water), which is typical of inorganic particles. A Junge power law similar to a phytoplankton size distribution is used. Pure seawater has scattering properties close to those of the Rayleigh phase matrix[24]: with a spectral dependence of $\lambda^{-4.3}$. The corresponding phase function varies as $\cos^2\theta$ and remains spectrally flat. Pope and Fry[25] described the absorption properties of pure seawater.

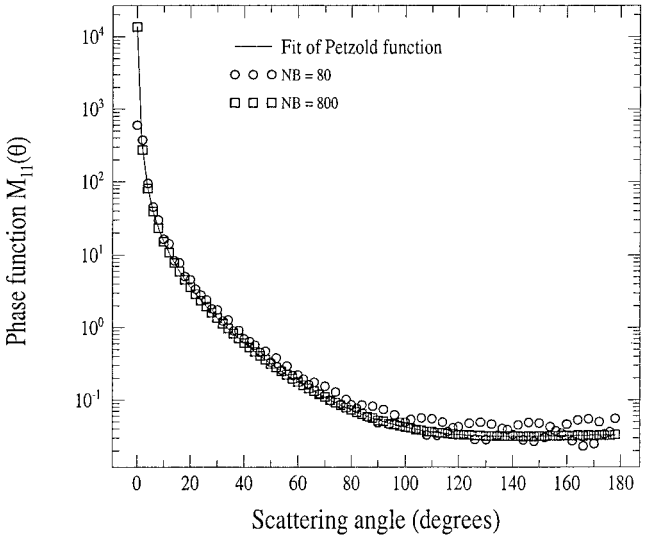

Fig. 4. Fit of the Petzold phase function[28] by a phase function obtained with particles modeled as being distributed according to a Junge size with a slope $\nu = -4$ and a refractive index $m = 1.23–0.162j$. The retrieval of the fitted function with a Legendre polynomial expansion is plotted for NB = 800 terms and NB = 80 terms. If the Legendre polynomial expansion is limited to NB = 80, the phase function oscillates.

The OSOA outputs the angular distribution of the radiance field. It is possible to select the radiometric quality (such as radiance, irradiance, diffuse reflectance, and bidirectional reflectance) and to display it as a function of depth if the user so desires. Here we study four observation points: at the bottom, just beneath the sea surface (0^-), just above the sea surface (0^+), and at the top of the atmosphere (TOA). All results are specified in the principal plane, and all computations were carried out on Silicon Graphics indigo IRIX 5.3 computers (~200 MHz).

B. Truncation

Truncation can occur when the phase function is highly peaked in the forward-scattering direction, such as for the marine particle phase function. The truncation procedure consists of assuming that the radiation diffracted in the peak is simply transmitted in the direction of the incident beam[26,27]; truncation has the effect of artificially reducing this peak. Consequently, scattering coefficient b must be modified as follows (see Appendix A):

$$b' = b \times (1 - f'), \tag{17}$$

where f' is the coefficient of truncation.

The necessity for truncation is illustrated in Fig. 4 with a Petzold particle phase function.[28] First, the Petzold phase function is fitted with Mie theory particles modeled as being distributed according to a Junge power law with a slope $\nu = -4$ and a refractive index $m = 1.23 - 0.162j$. This function can be accurately retrieved with 800 coefficients of Legendre

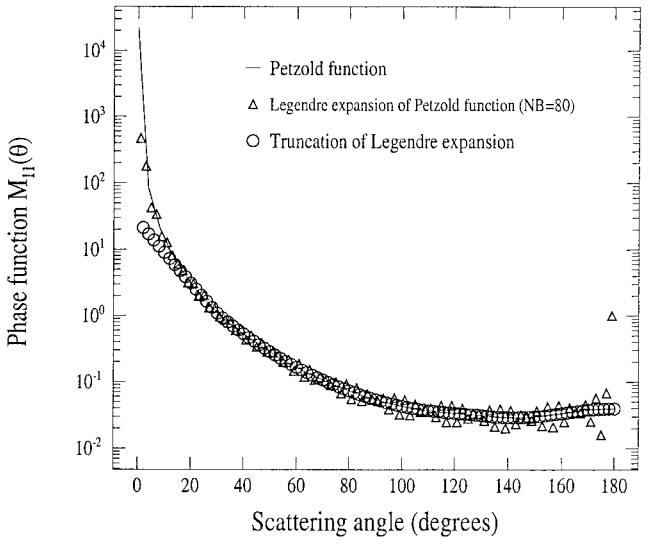

Fig. 5. Truncation of the Legendre polynomial expansion of the marine particle phase function measured by Petzold.[28] Truncation improves the accuracy of the Legendre phase function at angles far from the forward peak.

expansion, but it requires a time-consuming computation. To speed up the OSOA, the phase function expansion is limited to a NB of 80 coefficients. In such a case, the nontruncated phase function obtained from Eq. (2a) fluctuates, especially in the backscattering direction (Fig. 4). Once the truncation is accomplished (Fig. 5), the fluctuations observed in the backscattering direction are removed. The truncation modifies the downward radiance in the forward-scattering peak but does not modify the backscattering region, as would be required for correctly retrieving the water-leaving radiance. To verify that the inaccurate modeling of the forward peak is not critical, we ran the OSOA with the Petzold phase function of Fig. 4 for a situation corresponding to exact retrieval of a phase function (i.e., for a Legendre expansion containing 800 coefficients) and for one corresponding to the truncation of a phase function (i.e., for a Legendre expansion containing 80 coefficients; Table 1). Results indicate that the irradiances are correctly retrieved and that consequently the marine reflectances are too. Also, as one can see from Table 1, the spherical fluxes are identical before and after truncation; this ensures that the photosynthetically active radiation computations will be correct.

The truncation procedure needs to be extended to each element of the scattering matrix (Appendix A). The principle is based on conservation of the degree of polarization before and after the truncation as illustrated by Eq. (18a). The same approach is used for matrix term M_{33} [Eq. (18b)]:

$$\frac{M_{12}(\theta)}{M_{11}(\theta)} = \frac{M^*_{12}(\theta)}{M^*_{11}(\theta)}, \tag{18a}$$

$$\frac{M_{33}(\theta)}{M_{11}(\theta)} = \frac{M^*_{33}(\theta)}{M^*_{11}(\theta)}, \tag{18b}$$

where M_{ij} are the terms of the scattering matrix before truncation and M_{ij}^* are the terms after truncation.

Equations (18) allow each term of the truncated scattering matrix to be derived if one knows the initial and the truncated phase functions. Figure 6 illustrates validation of the correct retrieval in polarized light of the degree of polarization after truncation.

C. Convergence Criteria

The convergence test described in Subsection 2.A is applied to the radiance signal at the top of each layer (atmospheric and oceanic) for each Gaussian angle used in the quadrature and for each Fourier series term. For the zeroth ($s = 0$) term, this test is also applied to the upward and downward radiances just below the water surface to permit the in-water diffuse reflectance to be computed.

We define six test cases to illustrate the convergence conditions:

(1) Pure seawater of optical depth $\tau = 30$ at 443 nm.

(2) Case (1) with 5 mg m^{-3} of phytoplankton uniformly distributed throughout the vertical profile.

Table 1. Computation of Diffuse Downward and Upward Irradiances Just Below the Surface by Use of the Actual Petzold Phase Function and the Corresponding Truncated Function for Three Chlorophyll Contents for Case I Waters[a]

	Downward Irradiance			Upward Irradiance		
Chlorophyll a (mg m^{-3})	Truncation	Exact	$\Delta E/E$ (%)	Truncation	Exact	$\Delta E/E$ (%)
0.5	0.09652	0.09697	+0.46	0.18448	0.18381	−0.36
1	0.13584	0.13640	+0.41	0.26177	0.26061	−0.44
2	0.18281	0.18352	+0.39	0.35524	0.35348	−0.49
	Hemispherical Downward Irradiance			Hemispherical Upward Irradiance		
0.5	0.29295	0.29321	+0.09	0.39777	0.39645	−0.33
1	0.40732	0.40745	+0.03	0.55744	0.55514	−0.41
2	0.54294	0.54295	+0.002	0.74852	0.74505	−0.46

[a]The solar zenith angle is 30°, and the wavelength is $\lambda = 560$ nm. Also shown is the hemispherical irradiance computed for each case and the relative error $\Delta E/E = E_{\text{exact}} - E_{\text{truncated}}/E_{\text{exact}}$, where E is the irradiance in percent.

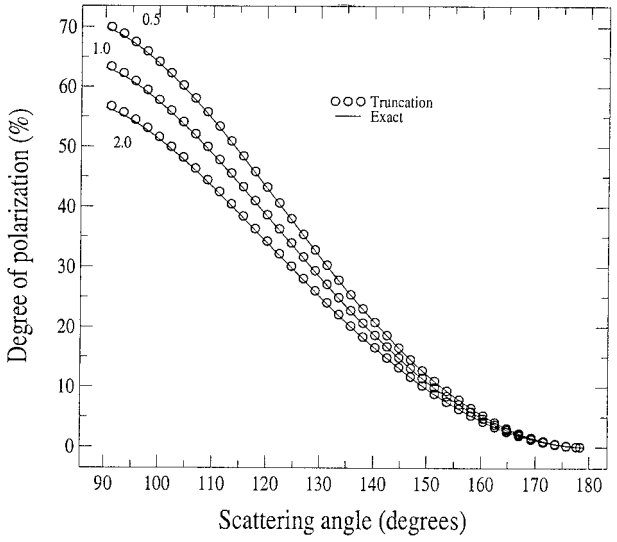

Fig. 6. Degree of polarization resulting from three chlorophyll contents (0.5, 1, and 2 mg m^{-3}) for the exact scattering matrix and the truncated matrix, as predicted by the OSOA. Results are reported for an observation point just beneath the sea surface (0^{-1}). The solar zenith angle is $\theta_0 = 0°$, and the wavelength is $\lambda = 560$ nm. Atmospheric effects are ignored.

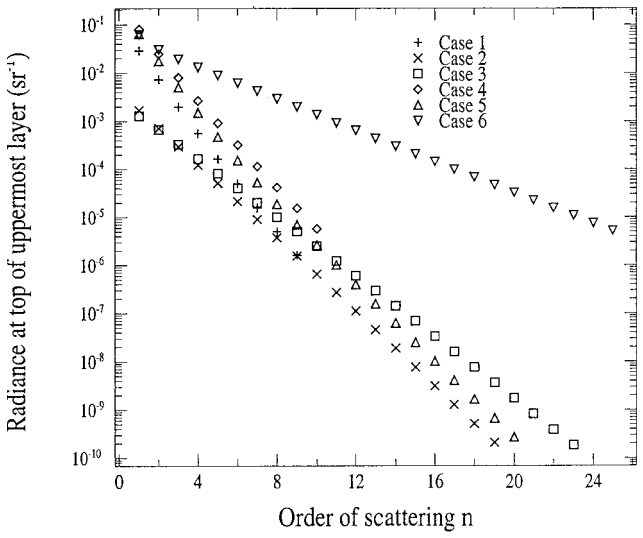

Fig. 7. Geometric series convergence of the upwelling radiance at the top of the uppermost layer for a nadir view. The solar zenith angle is $\theta_0 = 30°$. Results are plotted for the cases enumerated in Subsection 3.C. The radiance is normalized to extraterrestrial irradiance E_0, so $L_{\text{normalized}} = L(\pi/E_0)$ [sr^{-1}]. A geometric series convergence is obtained when the radiance values are lined up on the y log scale.

(3) Case (3) case (2) recomputed at 570 nm.

(4) Case (1) with a molecular atmosphere of optical thickness $\tau_r = 0.244$.

(5) Case (2) with a molecular atmosphere of optical thickness $\tau_r = 0.244$.

(6) Case (1) with 10 mg m^{-3} of phytoplankton homogeneously distributed along the vertical profile, with an atmosphere containing maritime aerosols (refractive index, 1.33–0.000j) of optical thickness $\tau_a = 0.8$ distributed following a Junge power law with a slope of -4.

Note that, in each of the first three cases, atmospheric layers are not considered. One can observe the convergence of the geometric series for these six cases by plotting the radiance signal as a function of the scattering order using a logarithmic scale. Figure 7 shows the radiance at the top of the uppermost layer (for the first three cases, this layer corresponds to the top of the ocean) at nadir observation for the zeroth term ($s = 0$) of the Fourier series. The radiance signal has been normalized by extraterrestrial irradiance $E_0 = \pi$ such that $L_N = L^*\pi/E_0$ [sr^{-1}]. The radiance rapidly decreases as the scattering order increases, even when the atmosphere is turbid. In general, higher orders of the Fourier series expansion tend to converge after fewer orders of scattering than do lower orders.

We use a separate convergence test to determine when to truncate the Fourier series expansion, i.e., for computational efficiency. This test is applied to the upwelled radiance in the specular direction (azimuth $\Phi = 180$), expressed as follows:

$$L(\mu_0, \mu, \phi = 180) = \sum_{s=0}^{\infty} (2 - \delta_{0s}) L^{(s)}(\mu_0, \mu). \quad (19)$$

Convergence is achieved when the contribution of a given term, s, is found to be sufficiently weak. In practice, the following threshold is employed:

$$2[L^{(s)}/L] < 10^{-3}. \quad (20)$$

For the six cases listed above, the order of convergence, both for the scattering order of the zeroth order ($s = 0$) Fourier series term and for Fourier series expansion, is summarized in Table 2.

D. Validation and Performances

Because numerous modifications were made to adapt the atmospheric version of the successive orders of scattering code for use with marine applications, validations of the resultant ocean layer radiance computations were performed and the numerical accuracy of the OSOA was tested.

Several comparisons of radiance with the radiative transfer model Hydrolight[8] were carried out. Because Hydrolight cannot account for the polarization effects, a scalar version of the OSOA was run. The first five cases summarized in Subsection 3.C were

Table 2. Order of Convergence for the Scattering Order of the Zeroth Order ($s = 0$) Fourier Series Term and for the Fourier Series Expansion ($\theta_0 = 30°$)[a]

	Case Number					
Order of	(1)	(2)	(3)	(4)	(5)	(6)
Scattering ($s = 0$)	9	19	23	10	20	25
Fourier series	3	23	23	3	23	33

[a]The six cases listed correspond to those enumerated in Subsection 3.C.

Table 3. Bidirectional Reflectance (in percent) Above the Ocean Surface, $\rho_w(0^+)$, for a Solar Zenith Angle of $\theta_0 = 30°$ and a Nadir View[a]

Radiative Transfer Model	Case Number (1)	(2)	(3)	(4)	(5)
OSOA scalar	2.38	0.405	0.530	2.54	0.630
	(9)	(38)	(42)	(9)	(38)
Hydrolight	2.37	0.425	0.566	2.58	0.656
	(68)	(434)	(433)	(711)	(436)
$\Delta\rho/\rho$ (%)	0.4	−4.9	−6.8	−1.6	−4.1

[a]Calculations were made with the scalar version of the OSOA code and with the Hydrolight model. The corresponding computation time (in seconds) is given in parentheses for the given case. The relative difference $\Delta\rho/\rho = (\rho_{OSOA} - \rho_{Hydrolight})/\rho_{OSOA}$ is also given. The five cases listed correspond to those enumerated in Subsection 3.C.

used for these comparisons. For each case, a solar zenith angle of 30° was used, along with a nadir view. The optical properties of phytoplankton are summarized in Subsection 3.A. The bidirectional reflectance ρ_w, defined by Lenoble,[29] was computed above the sea surface (0^+):

$$\rho_w(\theta_0, \theta_v, \Phi) = \frac{\pi L_w(\theta_0, \theta_v, \Phi)}{E_d}, \tag{21}$$

where E_d is the downward flux at sea level.

The results of the OSOA and Hydrolight computations are summarized in Table 3. For cases (1) and (4), which do not include any biomaterial, the two models agree closely (the relative errors are less than 2%). When the suspended matter is included in the water column, significant relative discrepancies are observed in the reflectance values computed by the two codes. Hydrolight reflectances are greater. Particles are responsible for anisotropy of the radiation, which increases the dependence of the comparisons on the angular quadratures used in the two respective codes. In the OSOA we carefully checked (Subsection 3.B) the retrieval of the particle phase function after truncation. In the Hydrolight the angular discretization is quite empirical (see Sects. 4.7 and 8.2 of Ref. 15) and is verified *a posteriori* on the basis of the normalization condition of the phase function. In our calculations this normalization was achieved to within a few percent, and that could explain the discrepancies. It is expected that a higher step in the angular discretization in the Hydrolight model will lead to results in better agreement with the OSOA but will also lead to a substantial increase in calculation time. However, it should be noted that the absolute difference in reflectance in the two models (Table 3) is within 0.04% and remains weak. Table 3 also presents the corresponding computation time for the two models. The OSOA code runs faster than the Hydrolight by a factor of 5–10, depending on the particular case. The OSOA is more efficient than numerical models such as those based on the Monte Carlo method, which require significantly more computations.

We used the principle of conservation of energy in the ocean–atmosphere system to assess the numerical accuracy of the OSOA. Conservative models were run, and the associated diffuse irradiances were computed. Calculations in which atmosphere was ignored were made with a solar zenith angle of $\theta_0 = 30°$, two optical thicknesses ($\tau = 5$ and $\tau = 30$), and two purely scattering media: isotropic (pure seawater) and particle (suspended sediments). For these trials, the reflectance of the ocean floor was set to be as much as 1. The relative difference between an ideal conservative case and the sum of the computed irradiances gives the numerical accuracy. These results are summarized in Table 4. For each case examined, the accuracy is better than 2%. Note that the order of scattering, n, is high, so the convergence process is quite slow. However, these cases are not realistic. Most natural waters are not dominated by scattering processes; i.e., they are not conservative. The addition of normal absorption effects substantially decreases the number of scattering events. For realistic cases it is therefore not unreasonable to expect improvement in accuracy by 1 order of magnitude compared with the results listed in Table 4.

As it was shown in Subsection 2.B, the Stokes formalism was extended to the oceanic layer to account for polarization of the underwater light field. Implementing the polarization is an undeniable asset in ocean color analyses. A polarized component of the underwater radiance signal may yield many new insights into problems that involve the retrieval of in-water constituents from remote-sensing measurements. Calibration algorithms

Table 4. Computations of Diffuse Irradiance for Conservative Cases[a]

Problem	Optical Depth	Number of Scattering Events n	Accuracy (%)
Pure seawater	5	582	1.8
	30	8587	1.7
Sediments	5	382	1.7
	30	3352	1.7

[a]The degree of accuracy expresses the relative difference between an ideal conservation result and the sum of the irradiances computed with the OSOA. The number of scattering events n required for the computation is indicated for each case.

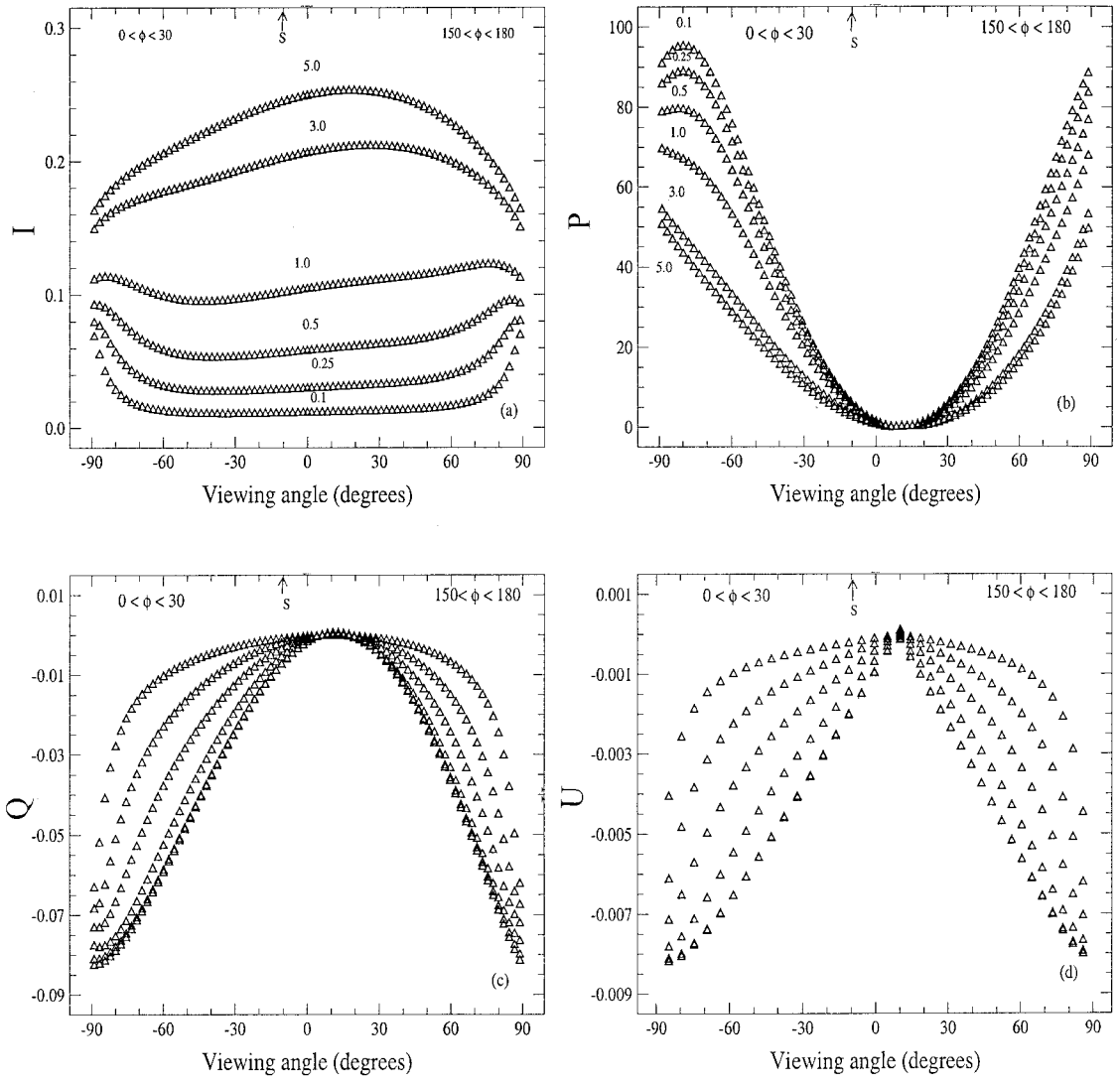

Fig. 8. (a) Reflected radiance, (b) degree of polarization, and (c) Stokes parameters Q and (d) U for models studied by Kattawar and Adams[30] (their Figs. 6 and 7). The results presented here were computed with the OSOA code for conservative scattering (single-scattering albedo, $\omega_0 = 1$), with molecularly scattering atmospheres with optical depths $\tau = 0.1, 0.25, 0.5, 1.0, 3.0$, and 5.0. The solar zenith angle (denoted S) is 10.24°. The results were averaged over the intervals $0° < \Phi < 30°$ (left) and $150° < \Phi < 180°$ (right).

that are capable of using the polarization properties of suspended matter to distinguish among the optical signatures of various constituents could significantly improve retrieval accuracy, as we discuss in Section 4 below. Certain computations were performed with the unmodified atmospheric code[14] to verify that the OSOA correctly handles polarization for the ocean–atmosphere system. Similar results were obtained for the two code versions. As an additional check, the OSOA outputs were compared with the results obtained by Kattawar and Adams with their Monte Carlo technique.[30] We carried out OSOA computations for cases identical to those described in their paper. The agreement in radiance as well as in degree of polarization was good. The results obtained by the OSOA are reproduced in Figs. 8 and 9 and are comparable with those of Kattawar and Adams.[30] Figure 8 is directly comparable with their Figs. 6 and 7; Fig. 9 is directly comparable with their Figs. 11 and 15. The physical analysis of these results is discussed by Kattawar and Adams.[30] Here our intent is merely to compare the two computational methods. The pertinent parameters used in these cases are summarized in the following two paragraphs.

For the results shown in Fig. 8, conservative scattering (i.e., single-scattering albedo, $\omega_0 = 1$) is assumed. The atmosphere is modeled as a pure molecular scattering medium that has optical depths of 0.1, 0.25, 0.5, 1.0, 3.0, and 5.0. The solar zenith angle is 10.24°. The plotted results (radiance, degree of polarization, Q and U Stokes parameters) were averaged over the intervals $0° < \Phi < 30°$ and $150° < \Phi < 180°$.

For the results shown in Fig. 9, the atmosphere–ocean system is separated by an interface of refractive index $n_w = 1.338$. The atmospheric optical depth is 0.15, and the oceanic optical depth is 4.85.

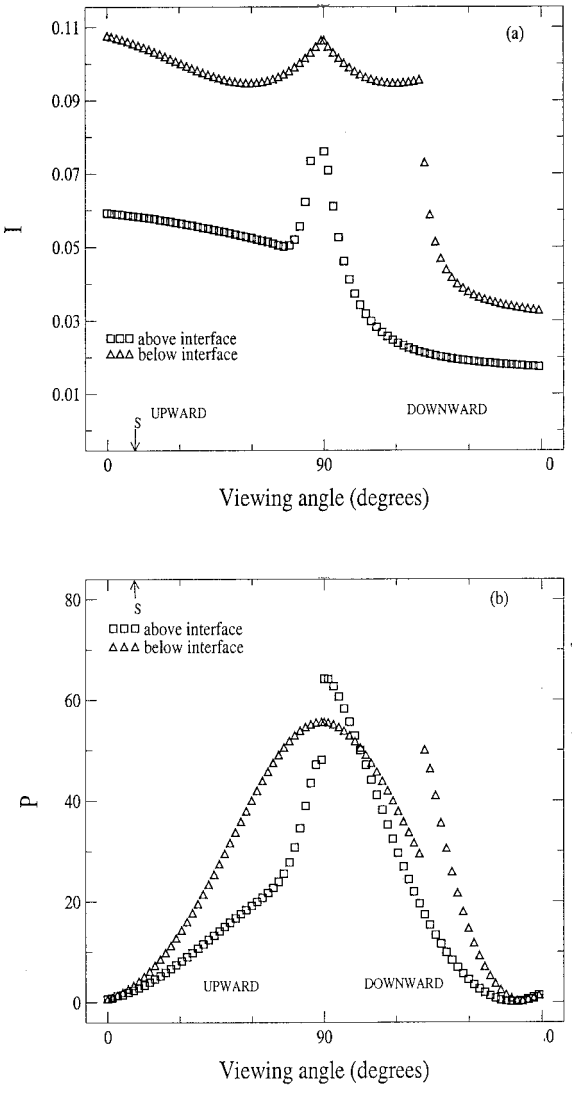

Fig. 9. (1) Upwelled and downwelled radiances and (b) degree of polarization for models studied by Kattawar and Adams[30] (their Figs. 11 and 15). The results presented here were computed with the OSOA code for an ocean–atmosphere system separated by an interface of refractive index $n_w = 1.338$. The atmosphere has an optical depth of 0.15, and the ocean has an optical depth of 4.85. Molecular scattering is used in each layer, and the single-scattering albedo is set to $\omega_a = 0.8$. Observations are made just above and just below the air–water interface. The solar zenith angle is 10.24°.

The scattering in all layers, atmospheric and oceanic, is modeled as being molecular, with a single-scattering albedo of $\omega_a = 0.8$. Computations are made just above and just below the air–water interface. The solar zenith angle is 10.24°. Upwelled and downwelled radiances and the degree of polarization are plotted.

The comparison has proved successful and supports the accuracy of the OSOA results. The error introduced when polarization is neglected was also evaluated. Cases (1)–(5) enumerated in Subsection 3.C were once again used for these evaluations. The resulting bidirectional reflectances computed above the sea surface for a nadir view, $\rho_w(0^+)$, are summarized in Table 5. For the first three cases, which do not include atmosphere, the difference between the two code versions is quite small, ranging from 2.1% for case (1) to 4.3% for case (3). The greater differences for cases (4) and (5) (10.0% and 9.2%, respectively), which include atmospheric influences, suggest that atmospheric polarization should be accounted for in radiance computations. The computation time required for the vectorized version of the code is approximately nine times longer than for the scalar version, which corresponds to the number of terms in the vector phase matrix. Nevertheless, even the vector-code runs are relatively short, seldom exceeding 15 min for standard cases. Therefore the inclusion of polarization effects does not decrease the performance of the OSOA model as substantially as for other models, especially Monte Carlo techniques.

4. Sensitivity of the Polarization to Hydrosols

The polarization of light in the ocean has been studied to a much lesser extent in the past decade than has the effect of the atmospheric polarization. There may be several reasons for this lack of knowledge about underwater polarization.

First, many technical problems can prevent the collection of reliable laboratory or *in situ* measurements. Sources of laboratory error include solid precipitation of suspended particles in the water column samples and spurious light sources that arise from reflection and scattering of light within an instrument. *In situ* measurements are subject to bioluminescence, various solar and atmospheric effects,

Table 5. Bidirectional Reflectance (in percent) Above the Ocean Surface, $\rho_w(0^+)$, for a Solar Zenith Angle of $\theta_0 = 30°$ and a Nadir View[a]

OSOA Version	Case Number (1)	(2)	(3)	(4)	(5)
OSOA scalar	2.38	0.405	0.530	2.54	0.630
	(9)	(38)	(42)	(9)	(38)
OSOA vector	2.43	0.417	0.554	2.31	0.577
	(69)	(161)	(495)	(77)	(319)
$\Delta\rho/\rho$ (%)	2.1	2.9	4.3	−10.0	−9.2

[a]Calculations were made with the scalar and the vector versions of the OSOA. The corresponding computation time (in seconds) is given in parentheses for the given case and code version. Relative differences $\Delta\rho/\rho = \rho_{vector} - \rho_{scalar}/\rho_{vector}$ are also given. The five listed cases correspond to those enumerated in Subsection 3.C.

scattering of the instrument beam by an adjacent water mass, and other perturbing effects. These processes and others result in unexpected errors that increase measurement uncertainty.

Second, knowledge of the state of water polarization requires measurement of all the Stokes parameters. This is seldom possible: It is often difficult enough to measure scalar submarine radiance accurately. Moreover, the oceanic scattering matrix has yet to be well quantified.[31] As a result, it is nearly impossible to describe the behavior of the coefficients of the matrix with respect to the concentrations of marine constituents.

Another factor that contributes to the lack of knowledge about oceanic polarization is that many of the most important oceanic processes, including photosynthesis, are believed to be independent of the polarization state of the light field. Nevertheless, polarization may have an important influence on the marine environment. Waterman[32] was among the first scientists to give consideration to this phenomenon. He showed that marine organisms ranging from zooplankton to fish use polarization to navigate under water. The polarization of light reflected from the sea surface also has applications in the field of remote sensing, including the analysis of atmospheric aerosols as is made by the Polarization and Directionality of Earth Reflectance (POLDER) experiment.[33] A SIMBAD astronomical database was recently developed at the Laboratoire d'Optique Atmosphérique of Lille, France, to measure polarized water-leaving radiance.[34] Coupling of SIMBAD and POLDER data should improve our knowledge of the polarization of light by the ocean.

However, the successive orders of the scattering method applied to the oceanic environment is a tool powerful enough to permit a theoretical study of the influences on polarization of marine particles such as phytoplankton and nonchlorophyllose matter. Here we describe simulations that were performed to study the effects of marine particles on the polarized component of a submarine radiance field. In addition, the consequences of such polarization effects on remotely sensed measurements are analyzed.

A. Conditions of the Computations

For all computations, the water-leaving signal was corrected for the reflection of the sky dome on the sea surface. For sea-surface measurements, this correction can be made with the well-known "quick and easy" procedure proposed by Carder and Steward[35] generalized to the polarized reflectance. For space observations, the atmospheric correction is a key point that is difficult to achieve over turbid waters. We shall omit addressing this problem, keeping in mind that the use of TOA polarized radiance will improve the characterization of the aerosols. Several predictions of total radiance and polarized radiance have been made. First, we studied models without any atmosphere to gain an understanding of the intrinsic polarized-signal signature of in-water particles. Subsequently we added the atmosphere to the model to better simulate realistic cases and to observe whether the simplified results were still valid.

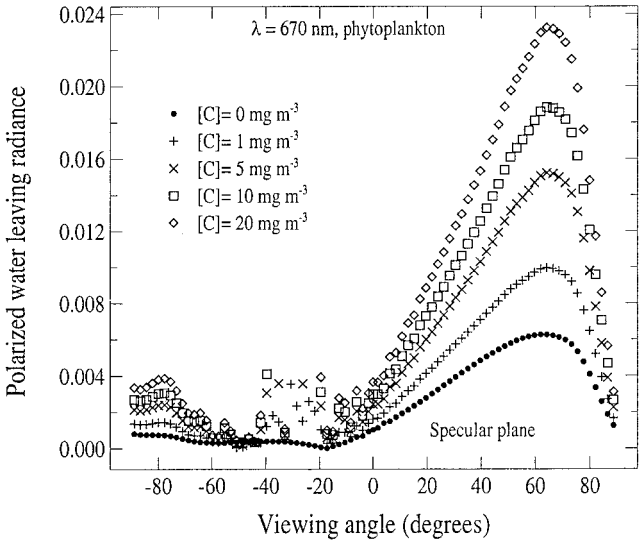

Fig. 10. Polarized water-leaving radiance for various concentrations of phytoplankton (here, 0, 1, 5, 10, and 20 mg m^{-3}) homogeneously distributed in the water column for the wavelength λ = 670 nm, as predicted by OSOA. The radiance is normalized to extraterrestrial irradiance E_0, so $L_{\text{normalized}} = L(\pi/E_0)$ [sr^{-1}; plotted data, 10^{-2} sr^{-1}]. The solar angle is $\theta_0 = 30°$, and atmospheric effects were ignored for the computations.

For the studies conducted, a number of assumptions and restrictions were made. Phytoplankton cells were modeled as being distributed according to a Junge power law (0.1 $\mu m < r < 50$ μm) with a slope $\nu = -3.2$ (corresponding to measurements made in the Straits of Dover) and a mean refractive index m = 1.05. The inherent optical properties of the cells were set according to bio-optical models used for case 1 waters.[21,22] The chlorophyll a concentrations used during successive trials were 0, 0.01, 0.03, 0.1, 0.3, 1.0, 3.0, and 5.0 mg m^{-3}. The associated vertical profile was modeled as being homogeneous or Gaussian.

Nonchlorophyllose matter (i.e., sediment) was also modeled as being distributed according to a Junge law (0.1 $\mu m < r < 50$ μm) with a flexible slope ν and a given refractive index m. The concentrations used in the successive trials were 0, 1, 5, 10, and 20 mg l^{-1}. The vertical profile was considered to be homogeneous.

B. Intrinsic Polarization Properties of Marine Chlorophyll

The intrinsic polarized properties of phytoplankton are analyzed with atmospheric effects ignored.

In coastal areas, only waters dominated by phytoplankton and their associated detritus (case 1 water conditions) can exist in homogeneous vertical distribution. Some computations of polarized water-leaving radiance in the principal plane were performed for a homogeneous profile. At long visible wavelengths, the magnitude of the signal is almost nonexistent (Fig. 10), even for high chloro-

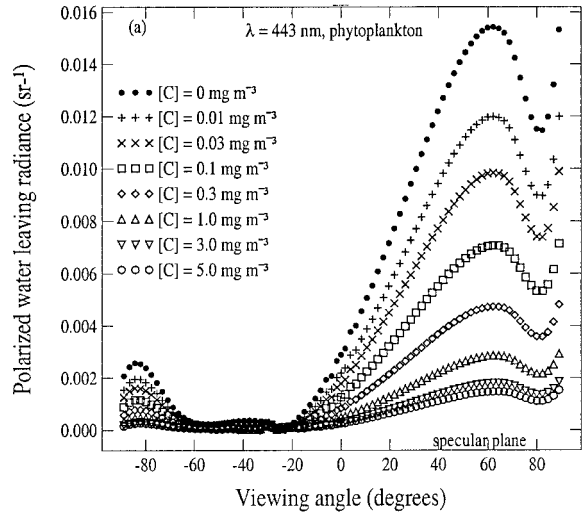

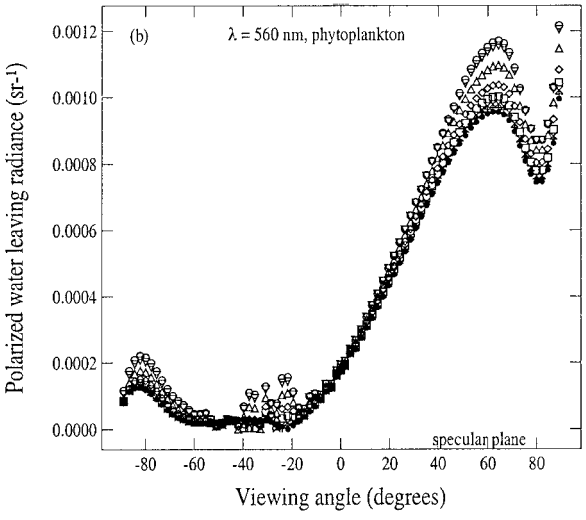

Fig. 11. Polarized water-leaving radiance computed in the principal plane for various phytoplankton concentrations homogeneously distributed in the water column (a) at 443 nm and (b) at 560 nm. Results are reported for an observation point above the sea surface (0^+). The solar zenith angle is $\theta_0 = 30°$, and atmospheric effects are ignored. Computational aspects for phytoplankton are enumerated in Subsection 4.A.

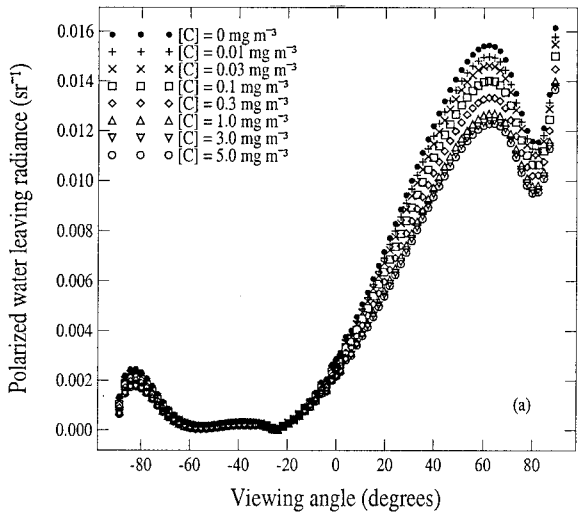

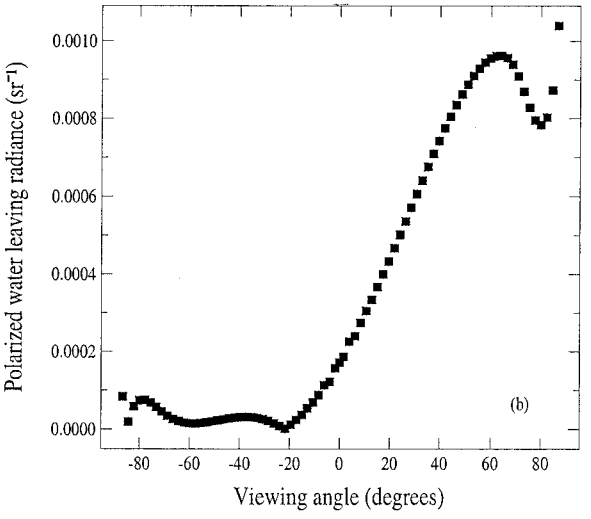

Fig. 12. Same as Fig. 11 but here a Gaussian distribution in the water column is selected for phytoplankton, with a deep chlorophyll maximum at $z_{max} = 80$ m.

phyll concentrations. In Fig. 11 the polarized radiance is plotted both in the blue (i.e., $\lambda = 443$ nm) and in the green (i.e., $\lambda = 560$ nm). The signal is weak in the green, and the influence of the phytoplankton is negligible. In the blue, because of its strong absorption, the phytoplankton depolarizes the pure seawater scattering. The same computations are shown in Fig. 12, still for case 1 water. The difference of Fig. 12 from Fig. 11 is that for the former a Gaussian vertical distribution of the chlorophyll was set with a deep chlorophyll maximum at an 80-m depth. The green polarized reflectance is completely independent of the chlorophyll content. In the blue, a weaker dependence on chlorophyll is observed with such a distribution. A molecularly polarized component is generated above the chlorophyll layer, so phytoplankton absorption is less sensitive to polarization. We conclude first that the water's polarized radiance in the green is due mainly to molecular scattering, so it is well predictable for ocean case 1 waters even if a homogeneous layer is treated. In the blue, this assumption is less relevant, especially when homogeneous vertical profiles are observed in coastal areas.

From the perspective of satellite missions, we now examine the contribution of marine and aerosol radiance to the signal received at the TOA. Simulations were performed at the TOA level at 443 and at 560 nm for two atmospheric conditions: a pure molecular atmosphere and a standard aerosol model. Inasmuch as we treat open ocean waters in this section, the atmosphere was modeled as consisting of maritime aerosols. The associated size distribution was modeled according to a Junge power law with a slope

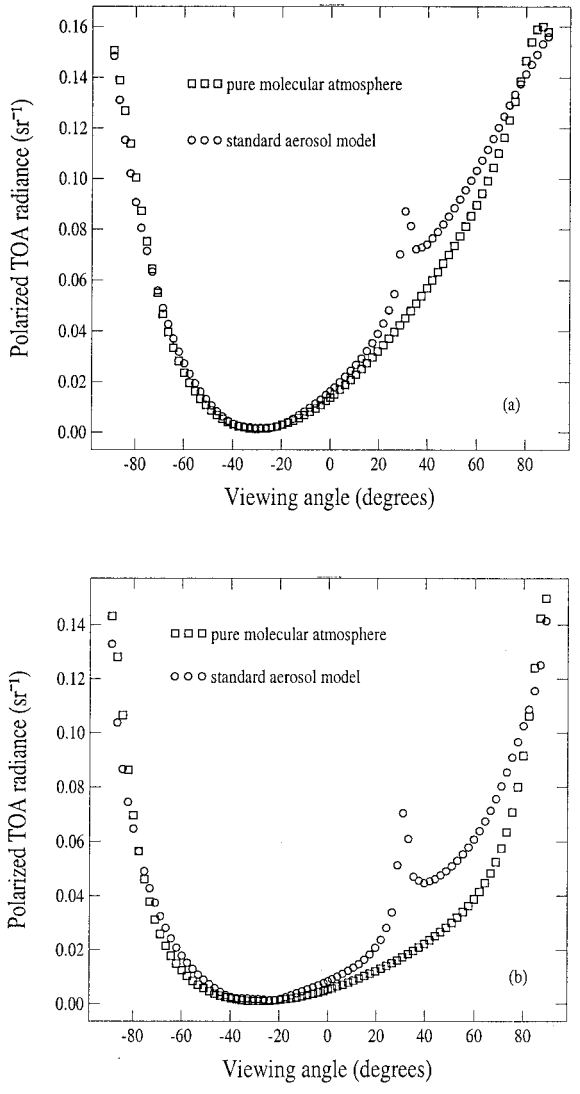

Fig. 13. Polarized TOA radiance for a phytoplankton concentration of 1 mg m^{-3} at (a) 443 nm and (b) 560 nm as predicted by the OSOA code. A Gaussian vertical profile (z_{max} = 80 m) is used for the phytoplankton. A pure molecular atmosphere and a standard aerosol model were computed. Aerosols were modeled as being distributed according to a Junge power law with a slope of $\nu = -4$, the refractive index is $m = 1.33–0.000j$, and the visibility is 23 km. The solar zenith angle is 30°.

of $\nu = -4$; the refractive index used was $m = 1.33–0.000j$, and the visibility was 23 km. The solar zenith angle was set to $\theta_0 = 30°$. A Gaussian vertical distribution was used for phytoplankton. Results are pictured in Fig. 13. Because variations in chlorophyll concentration appeared to be extremely small, polarized radiance was plotted for a concentration of 1 mg m^{-3} for clarity. Figure 13 shows that the aerosol contribution is quite weak at 443 nm. Note that, for homogeneous vertical profiles, a dependence of the signal on chlorophyll concentration can occur. Conversely, at 560 nm, the TOA polarized signal makes apparent the aerosol signature. As the ocean's polarized radiance is independent of chlorophyll content and distribution at this wavelength

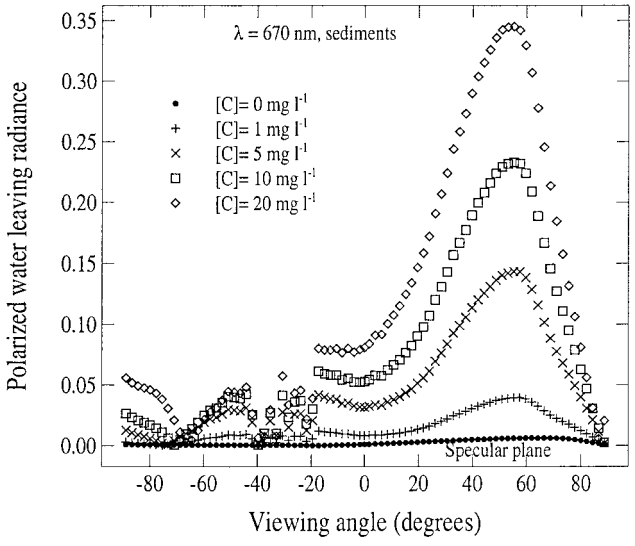

Fig. 14. Polarized water-leaving radiance resulting from various concentrations of sediment at λ = 670 nm, as predicted by the OSOA code. The radiance is normalized to extraterrestrial irradiance E_0, so $L_{normalized} = L(\pi/E_0)$ [sr^{-1}; plotted data, units of 10^{-2} sr^{-1}]. The solar angle is $\theta_0 = 30°$, and atmospheric effects were ignored for the computations. Computational conditions for sediments are enumerated in Subsection 4.A. The refractive index is $m = 1.20–0.001j$, and slope ν is −3.2.

(Figs. 11 and 12), it is shown here that a polarized signal should be a complementary measurement to that of total reflectance in deriving aerosol properties that lead to improvements in atmospheric correction schemes.

C. Intrinsic Polarization Properties of Marine Sediments

First, atmospheric effects are ignored. The solar angle is $\theta_0 = 30°$ and the observation is made above the sea surface (0^+) at all viewing angles. The polarized water-leaving radiance has been normalized by extraterrestrial irradiance $E_0 = \pi$, such that $L_{wN} = L_w^*\pi/E_0$ [sr^{-1}]. As we discussed above (Fig. 10), phytoplankton is not polarized much in the red. So the optimum optical signature of the sediment should be dissociated from the influence of yellow substances and chlorophyll at long visible wavelengths. Sediments that were modeled with a slope of $\nu = -3.2$ and a refractive index $m = 1.20–0.001j$ produce a signal approximately 1 order of magnitude greater than that of phytoplankton at these longer wavelengths, with maximum values of 3×10^{-3} at 670 nm (Fig. 14). At 670 nm, it might be possible to discriminate sediment from phytoplankton by use of the differences in polarized radiance of these two constituents and after correction for the phytoplankton contribution after the chlorophyll content has been estimated by classical algorithms.

If characteristics of the sediments, such as size distribution and refractive index, are known, the sediment concentration could be derived by use of water-leaving radiance at 670 nm, assuming a standard vertical profile. Accounting for polarized radiance could provide additional information. The maxi-

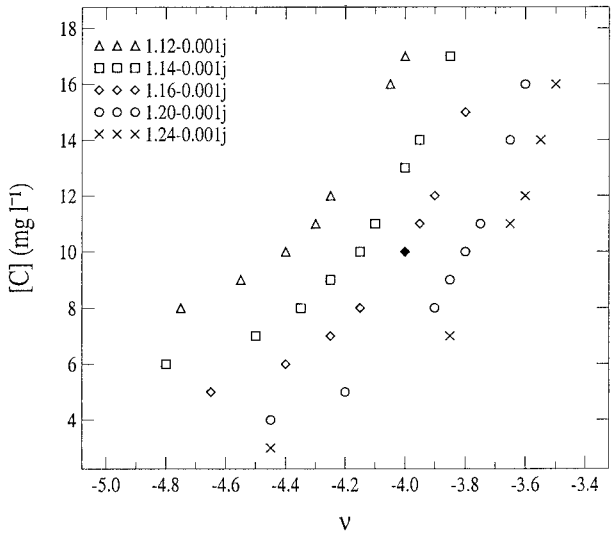

Fig. 15. Relationship between sediment concentration and slope ν of sediment size distribution for several sediment refractive indices. The total Rrs was computed by the OSOA code for a scattering angle $\theta = 100°$, for an observation point above the sea surface (0^+), and for a solar zenith angle of 30°. Atmospheric effects were ignored. A sediment reference model was selected. In this reference model, sediment is distributed according to a Junge power law size distribution with a slope of $\nu = -4$, the refractive index is $m = 1.16–0.001j$, and the concentration is $C = 10$ mg/l (filled diamond). Only sediment models that successfully retrieved the total reference Rrs are plotted.

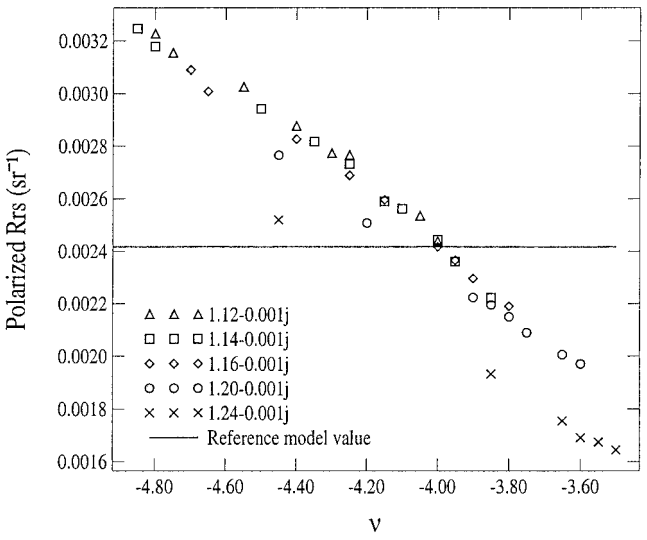

Fig. 16. Polarized remote-sensing reflectance Rrs that correspond to the sediment models that permit retrieval of the total reference Rrs (Fig. 15) as computed by the OSOA code. Computational conditions are similar to those for Fig. 15. The horizontal bar indicates the polarized Rrs value obtained with the reference sediment model. The polarized component enables one to select from among the numerous models that retrieve the total Rrs signal.

mum of polarized radiance occurs near a scattering angle of $\theta = 100°$. Computations of the total and the polarized remote-sensing reflectance ratio between upward radiance and downward irradiance, (Rrs) were performed at at 670 nm for one sediment model, which we call the reference model. In this model, sediments were distributed according to a Junge law with a slope of $\nu = -4$; the refractive index was $m = 1.16–0.001j$, and the concentration was $C = 10$ mg l^{-1}, where C is the concentration. Observations were made at a scattering angle of $\theta = 100°$ above the sea surface.

We then conducted trials for different sediment models, attempting to match the total Rrs given by the reference model. Sediment models involved a variation of refractive index m from 1.12 to 1.24, a variation of slope ν from -3.8 to 5, and a variation of concentration C from 1 to 20 mg l^{-1}. Figure 15 illustrates the sediment models that successfully retrieve the total reference Rrs. Many models could be used, and it is not possible to derive the sediment concentration correctly. Given a refractive index m, Fig. 15 shows that the sediment concentration decreases with ν; in other words, given total Rrs, small particles do not need to be so concentrated as large particles. This is so because of the particle phase function, which increases for small hydrosols in a backscattering region tending to a Rayleigh–Gauss regime. Once refractive index m is set, a relationship between ν and C is obtained.

Subsequently, polarized Rrs that corresponded to the successful sediment models were compared (Fig. 16). The horizontal line indicates the value provided by the reference model. Only few models match. Polarized Rrs then allows ν, and therefore C, to be obtained. The unknown remains m, but usually this parameter can be assumed for a given area when one knows the geological composition of the sediment. So, unlike the total Rrs, the polarized component of the signal permits selection among various sediment models and could be a key parameter to retrieval of sediment properties.

Finally, we investigate the influence of the atmosphere on the water-leaving signal. Coupling between atmosphere and ocean influences the polarized radiance less than the total radiance. In the case that we now examine, atmospheric effects are no longer ignored. The atmosphere was modeled as consisting of classical continental aerosols for coastal zones. The associated size distribution was modeled according to a Junge law with a slope of $\nu = -4.0$, the refractive index used was $m = 1.50–0.001j$, the solar angle used was 30°, and the visibility was 8 km. Figure 17 is plotted for conditions of computation similar to those of Fig. 14, except that atmosphere is included. The atmospheric radiance reflected by the sea surface has been removed from the radiance at sea level (0^+) to produce a water-leaving radiance. The shape of the polarized water-leaving radiance when the atmosphere is accounted for is quite similar to the results in Fig. 14. Only the values are weaker in Fig. 17. This result can be explained as follows: In one case [Fig. 14] the ocean is illuminated only by a direct solar beam, whereas in the second case [Fig.

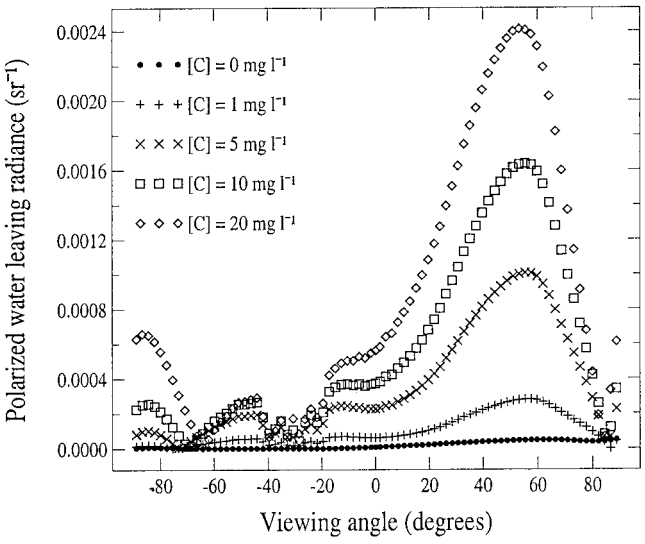

Fig. 17. Same as Fig. 14, except that atmospheric effects are included. The aerosol was modeled as being distributed according to a Junge power law with a slope of $\nu = -4$, the refractive index is $m = 1.50–0.001j$, and the visibility is 8 km. The polarized water-leaving radiance plotted here has been corrected for the sky reflection on the sea surface.

17] the diffuse sky radiance that is due to aerosols also contributes to the downward irradiance at the sea surface. Because the diffuse sky radiance does not generate water-leaving polarization (except in the forward peak, which can be assimulated by the direct solar irradiance), the direct solar beam is simply attenuated by the downward atmospheric path, leading to a decrease of the polarized signal in Fig. 17. As an illustration, the ratio of polarized water-leaving radiances when atmosphere is accounted for and when atmosphere is ignored in the specular plane is plotted in Fig. 18. This ratio is ~0.7 and is close to the extinction value of direct solar beam by aerosols, which is $\exp(-\tau_a/\mu_0)$ (τ_a = 0.422 at 670 nm for a visibility of 8 km). Moreover, the ratio does not depend on the water content (i.e., sediment concentration). So, given an atmospheric condition, the polarized water-leaving radiance at sea level could be easily corrected for the atmospheric influence to permit retrieval of the intrinsic signature of marine particles.

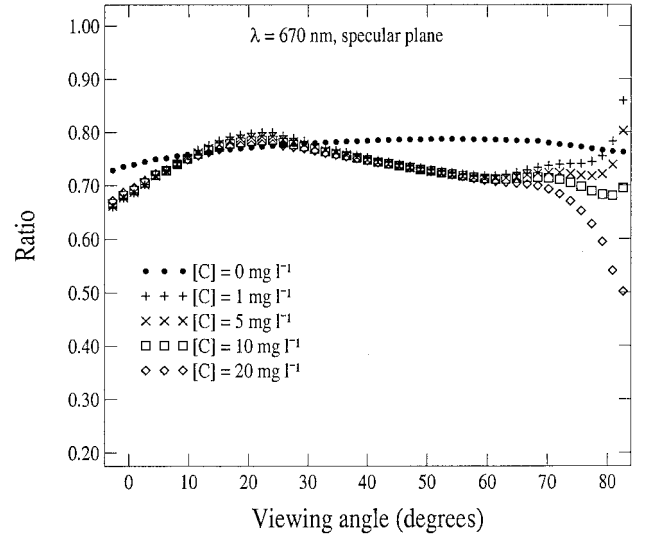

Fig. 18. Ratio of polarized water-leaving radiance when atmospheric effects are accounted for (Fig. 17) and ignored (Fig. 14) for several sediment concentrations in the specular plane. Briefly, the existence of the atmosphere modifies the downward incoming ocean irradiance (extinction of direct solar beam, diffuse flux). The effect on the polarized water-leaving radiance is observed here.

5. Conclusion

In this paper a radiative transfer model adapted for the atmosphere–ocean system OSOA has been presented. This model was created through modification of an existing atmospheric code that uses the successive orders of a scattering method to solve the radiative transfer equation. Major advantages of this method are its representation of the radiance field in terms of an azimuth Fourier series expansion and the generation of a separate analytical formulation for each zenith component. In principle, the successive orders of the scattering method are not necessarily adaptable to an infinite medium, such as the ocean. However, absorption effects and the convergence of the radiance field into a geometric series limit the number of scattering computations required. In the OSOA, an oceanic layer is included; it enables the radiance contributions that arise from a given amount of suspended matter, e.g., phytoplankton, sediment, and yellow substances, in the water column to be predicted. Empirical bio-optical models defined by earlier studies have been used to assign realistic optical properties to particulate concentrations. Once they are truncated, the Legendre-expanded particle phase functions are accurately modeled. Moreover, several aerosol models, e.g., Junge laws and Shettle models, can be selected. Like the original atmospheric code, the OSOA model makes use of the Stokes formalism to describe the light field, so the polarization state of the signal is taken into account. A rigorous validation of the OSOA code was carried out through comparisons with standard ocean–atmosphere models. The high computational efficiency (notwithstanding the inclusion of polarization) and high numerical accuracy (an error of less than 2% for even the most unrealistic, taxing cases) make the OSOA model flexible and powerful.

Therefore the model is applicable for sensitivity studies of oceanic environments and for analyzing the polarization properties of various atmospheric and oceanic constituents. The OSOA permits the computation of the optical properties of individual marine components, although assumptions made about these constituents (sphericity of particles, use of a mean refractive index, etc.) must be kept in mind. Unless the phase functions of these marine particles are accurately measured, such approximations will need to be made.

Applications of the OSOA code to oceanic remote-sensing problems were also provided in this paper. Algorithms for retrieval of suspended matter should be improved for case 2 waters, especially when polarized information is used. A preliminary study has been presented to illustrate the access to sediment characterization by use of a polarized signal at 670 nm. A more extensive study should be conducted that would include other spectral bands, and specific attention should be paid to atmospheric correction. Also, for ocean case 1 waters, a recommendation has been made to use the polarized reflectance at 560 nm to improve the aerosol characterization.

Possible extensions of the method include computation of inelastic scattering effects related to phenomena such as Raman scattering and fluorescence and the introduction of a windblown surface to simulate the effects of sea-surface roughness. Modeling the air–water interface as an infinitely thin layer permits the inclusion of a windblown surface: The reflection matrix should be rewritten to account for the corresponding wave slope distribution. However, these extensions will require modifications of the OSOA and are deferred to future studies.

Appendix A. Comments about the Procedure for Truncation of the Phase Matrix

The phase matrix terms are expanded in Legendre polynomials. Because the computing time depends on the length of the expansion, it is quite interesting to limit the number of Legendre terms. Therefore we truncate the phase matrix. First we describe the procedure for truncating the phase function (term M_{11} of the phase matrix) and then we extend this procedure to the phase matrix, which includes the polarization state of the light.

1. Procedure for Truncating Phase Function M_{11}

Particle phase function M_{11} is highly forward peaked, in accordance with diffraction theory. The exact retrieval of such a function with Legendre polynomials requires numerous terms (almost 800) mainly to ensure correct retrieval of the forward peak. In the approximation of the truncation, the radiation diffracted in the peak is assumed to be simply transmitted in the direction of incident beam.[26,27] Truncation consists in reducing this peak, extrapolating M_{11} between a given scattering angle and 0°. Consequently truncation leads to a new phase function M_{11}^*, which can be correctly retrieved with many fewer (80) Legendre terms.

Let us consider radiant flux ψ scattered by a small volume dV over all directions. Such a flux is written [see Eq. (1.49) of Ref. 29] as

$$\psi = \frac{b\,\mathrm{d}VE_0}{4\pi}\int_0^{2\pi}\int_{-1}^{+1} M_{11}(\mu)\,\mathrm{d}\mu\,\mathrm{d}\phi, \qquad \text{(A1)}$$

where Φ is the azimuth angle, μ is the cosine of the zenith angle, E_0 is the incident irradiance, and b is the scattering coefficient. Truncation involves a modification of the scattered flux toward small-scattering angles. When M_{11}^* instead of M_{11} is used, the amount of scattered flux that is missing in the forward peak region is expressed as follows:

$$\psi' = \frac{b\,\mathrm{d}VE_0}{4\pi}\int_0^{2\pi}\int_{-1}^{+1} [M_{11}(\mu) - M_{11}^*(\mu)]\,\mathrm{d}\mu\,\mathrm{d}\phi. \qquad \text{(A2)}$$

Introducing coefficient A:

$$A = \int_{-1}^{+1} [M_{11}(\mu) - M_{11}^*(\mu)]\,\mathrm{d}\mu, \qquad \text{(A3)}$$

we can write ψ' as

$$\psi' = b\,\mathrm{d}VE_0(A/2). \qquad \text{(A4)}$$

When truncation is performed, flux ψ' is taken into account within the direct (i.e., unscattered) beam. Mathematically, the extinction of the incident irradiance is then modified after truncation as follows:

$$\mathrm{d}E = -b\,\mathrm{d}VE_0\left(1 - \frac{A}{2}\right). \qquad \text{(A5)}$$

The attenuation of the direct incident beam is less when the truncation is applied. That leads to a decrease in scattering coefficient b as follows:

$$b^* = b(1 - f'), \qquad \text{(A6)}$$

where $f' = A/2$; f' is the coefficient of truncation.

Moreover, single-scattering albedo ω_a and optical thickness τ, which are dependent of b, are also modified:

$$\omega_a^* = \frac{\omega_a(1 - f')}{1 - \omega_a f'}, \qquad \text{(A7)}$$

$$\tau^* = \tau(1 - \omega_a f'). \qquad \text{(A8)}$$

The radiant scattered flux is expressed after truncation:

$$\psi^* = \frac{b^*\,\mathrm{d}VE_0}{4\pi}\int_0^{2\pi}\int_{-1}^{+1} M_{11}^t(\mu)\,\mathrm{d}\mu\,\mathrm{d}\phi, \qquad \text{(A9)}$$

where $M_{11}^t = M_{11}^*/(1 - f')$ with respect to the following criterion of normalization [according to Eq. (A3)]:

$$\int_{-1}^{+1} M_{11}^t(\mu)\,\mathrm{d}\mu = 2. \qquad \text{(A10)}$$

2. Extension of the Procedure for Polarized Light

We extend the previous procedure for polarized light, taking into account each term of phase matrix $\tilde{M}$.[36] In primary scattering, $\tilde{M}$, developed in Legendre

polynomials P_l and associated functions P_l^2, has the form [see Eq. (6) of Ref. 14].

$$\tilde{M} = \begin{bmatrix} M_{11} = \sum_{l=0}^{\mathrm{NB}} \beta_l P_l(\mu) & M_{12} = \sum_{l=2}^{\mathrm{NB}} \gamma_l P_l^2(\mu) & 0 \\ M_{12} = \sum_{l=2}^{\mathrm{NB}} \gamma_l P_l^2(\mu) & M_{11} = \sum_{l=0}^{\mathrm{NB}} \beta_l P_l(\mu) & 0 \\ 0 & 0 & M_{33} = \sum_{l=0}^{\mathrm{NB}} \delta_l P_l(\mu) \end{bmatrix}, \tag{A11}$$

where β_l, γ_l, and δ_l are Legendre coefficients and NB is the length of development.

The problem consists of replacing this matrix with a new one, $\tilde{M}^*$, whose elements are expanded in fewer Legendre terms NB* such as to obtain similar results. As we explained in Subsection 6.A, truncation of phase function M_{11} involves a decrease of the scattered flux in the forward peak, which is taken into account within coefficient b^* [Eq. (A6)]. Nevertheless, in primary scattering, the degree of polarization needs to keep the same value that it had before truncation. The conservation of the degree of polarization is then expressed as

$$\frac{\sum_{l=2}^{\mathrm{NB}} \gamma_l P_l^2(\mu)}{\sum_{l=0}^{\mathrm{NB}} \beta_l P_l(\mu)} = \frac{\sum_{l=2}^{\mathrm{NB}^*} \gamma_l^* P_l^2(\mu)}{\sum_{l=0}^{\mathrm{NB}^*} \beta_l^* P_l(\mu)}. \tag{A12}$$

Legendre coefficients β_l^* were calculated when the phase function was truncated into M_{11}^*. Inasmuch as the elements of the original phase matrix, M_{11}, M_{12}, and M_{33}, are known, the Legendre coefficients γ_l^* of M_{12}^* are easily obtained [Eq. A12]. In the same way, we have

$$\frac{M_{33}(\mu)}{M_{11}(\mu)} = \frac{M_{33}^*(\mu)}{M_{11}^*(\mu)}, \tag{A13}$$

which provides coefficients δ_l^* for the matrix element M_{33}^*.

References

1. C. Cox and W. Munk, "Measurement of the roughness of the sea surface from photographs of the Sun's glitter," J. Opt. Soc. Am. **44,** 838–850 (1954).
2. G. N. Plass and G. W. Kattawar, "Color of the ocean," Appl. Opt. **17,** 1432–1446 (1978).
3. H. R. Gordon and O. B. Brown, "Irradiance reflectivity of a flat ocean as a function of the optical properties," Appl. Opt. **12,** 1549–1551 (1973).
4. M. Viollier, "Contribution à l'étude du rayonnement rétrodiffusé par l'océan. Application à la télédétection de la chlorophylle," Ph.D. dissertation (Université des Sciences et Techniques de Lille, Lille, France, 1976).
5. H. Gordon, "A bio-optical model describing the distribution of irradiance at the sea surface resulting from a point source embedded in the ocean," Appl. Opt. **26,** 4133–4148 (1987).
6. C. D. Mobley, B. Gentili, H. R. Gordon, J. Zhonghai, G. W. Kattawar, A. Morel, P. Reinersman, K. Stamnes, and R. H. Stavn, "Comparison of numerical models for computing underwater light fields," Appl. Opt. **32,** 7484–7504 (1993).
7. A. Morel and B. Gentili, "Diffuse reflectance of oceanic waters. II. Bidirectional aspects," Appl. Opt. **32,** 6864–6879 (1993).
8. C. D. Mobley, "A numerical model for the computation of radiance distributions in natural waters with wind-roughened surfaces," Limnol. Oceanogr. **34,** 1473–1483 (1989).
9. G. N. Plass and G. W. Kattawar, "Radiative transfer in an atmosphere–ocean system," Appl. Opt. **8,** 455–466 (1969).
10. E. Raschke, "Multiple scattering calculation of the transfer of solar radiation in an atmosphere–ocean system," Contrib. Atmos. Phys. **45,** 1–19 (1972).
11. G. N. Plass and G. W. Kattawar, "Monte Carlo calculations of radiative transfer in the Earth's atmosphere–ocean system. I. Flux in the atmosphere and the ocean," J. Phys. Oceanogr. **2,** 139–145 (1972).
12. Z. Jin and K. Stamnes, "Radiative transfer in nonuniformly refracting layered media such as the atmosphere–ocean system," Appl. Opt. **33,** 431–443 (1994).
13. H. R. Gordon and T. Zhang, "How well can radiance reflected from the ocean–atmosphere system be predicted from measurements at the sea surface?," Appl. Opt. **35,** 6527–6543 (1996).
14. J. L. Deuzé, M. Herman, and R. Santer, "Fourier series expansion of the transfer equation in the atmosphere–ocean system," J. Quant. Spectrosc. Radiat. Transfer **41,** 483–494 (1989).
15. C. D. Mobley, *Light and Water* (Academic, San Diego, Calif., 1994).
16. J. L. Deuzé, "Etude de la polarisation du rayonnement par les milieux diffusants. Application à la polarisation localisée de Venus," Ph.D. dissertation (Université des Sciences et Techniques de Lille, Lille, France, 1974).
17. E. Dilligeard, "Télédétection des eaux du cas II. Caractérisation des sédiments marins," Ph.D. dissertation (Université du Littoral Côte d'Opale, Wimereux, France, 1997).
18. A. Bricaud, A. Morel, and L. Prieur, "Absorption by dissolved organic matter of the sea (yellow substance) in the UV and visible domains," Limnol. Oceanogr. **26,** 43–53 (1981).
19. A. Morel, "Optical modeling of the upper ocean in relation to its biogenous matter content (case 1 waters)," J. Geophys. Res. **93,** 10,749–10,768 (1988).
20. H. R. Gordon and A. Morel, *Remote Assessment of Ocean Color for Interpretation of Satellite Visible Imagery. A Review*, Vol. 4 of Lecture Notes on Coastal and Estuarine Studies (Springer-Verlag, New York, 1983).
21. H. Bader, "The hyperbolic distribution of particle sizes," J. Geophys. Res. **75,** 2822–2830 (1970).
22. C. H. Whitlock, L. R. Poole, J. W. Usry, W. M. Houghton, W. G. Witte, W. D. Morris, and E. A. Gurganus, "Comparison of

reflectance with backscatter and absorption parameters for turbid waters," Appl. Opt. **20,** 517–522 (1981).
23. Y. H. Ahn, "Propriétés optiques de particules biologiques et minérales présentes dans l'océan. Application: inversion de la réflectance," Ph.D. dissertation (Université Pierre et Marie Curie, Paris, 1990).
24. A. Morel, "Optical properties of pure water and pure seawater," in *Optical Aspects of Oceanography*, N. G. Jerlov and N. E. Steemann eds. (Academic, San Diego, Calif., 1974).
25. R. M. Pope and E. S. Fry, "Absorption spectrum (380–700 nm) of pure water. II. Integrating measurements," Appl. Opt. **36,** 8710–8723 (1997).
26. J. Potter, "The delta function approximation in radiative transfer theory," J. Atmos. Sci. **27,** 943–949 (1970).
27. J. Lenoble, ed., *Standard Procedures To Compute Atmospheric Radiative Transfer in a Scattering Atmosphere* (International Association of Meteorology and Atmospheric Physics Radiation Commission, 1974), Vols. I and II.
28. T. J. Petzold, "Volume scattering functions for selected natural waters," in *Light in the Sea*, J. E. Tyler, ed. (Dowden, Hutchinson and Ross, Stroudsberg, Pa., 1977), pp. 150–174.
29. J. Lenoble, *Atmospheric radiative transfer* (Deepak, Hampton, Va., 1993).
30. G. W. Kattawar and C. N. Adams, "Stokes vector calculations of the submarine light field in an atmosphere–ocean system with scattering according to a Rayleigh phase matrix: effect of interface refractive index on radiance and polarization," Limnol. Oceanogr. **34,** 1453–1472 (1989).
31. K. J. Voss and E. S. Fry, "Measurements of the Mueller matrix for ocean water," Appl. Opt. **23,** 4427–4439 (1984).
32. T. H. Waterman, "Polarization patterns in submarine illumination," Science **120,** 927–932 (1954).
33. P. Y. Deschamps, M. Herman, F. M. Bréon, M. Leroy, A. Podaire, A. Bricaud, J. C. Buriez, and G. Sèze, "The POLDER mission: instrument characteristics and scientific objectives," IEEE Trans. Geosci. Remote Sens. **32,** 3598–3615 (1994).
34. B. Fougnie, "Contribution à l'observation de la couleur de l'océan à partir du capteur spatial POLDER," Ph.D. dissertation (Université des Sciences et Techniques de Lille, Lille, France, 1998).
35. K. L. Carder and R. G. Steward, "A remote-sensing reflectance model of a red tide dinoflagellate off West Florida," Limnol. Oceanogr. **30,** 286–298 (1985).
36. R. Santer, "Contribution à l'étude de la polarisation du rayonnement solaire diffusé par Vénus," Ph.D. dissertation (Université des Sciences et Techniques de Lille, Lille, France, 1977).